

Cite this: *J. Mater. Chem. A*, 2016, 4, 12658

Graphene/nitrogen-doped porous carbon sandwiches for the metal-free oxygen reduction reaction: conductivity versus active sites†

M. Qiao,^{†a} C. Tang,^{†ab} G. He,^c K. Qiu,^c R. Binions,^{ad} I. P. Parkin,^c Q. Zhang,^{ab} Z. Guo^c and M. M. Titirici^{*ad}

The oxygen reduction reaction (ORR) plays a critical role in sustainable energy systems. Among the most promising metal free ORR electrocatalysts, nitrogen-doped carbon materials have generated significant research interest. Nitrogen doping within a graphitic/turbostratic network of carbon atoms generates active sites for the ORR via C–N bond polarisation that induces a reduced energy barrier towards the ORR on the adjacent carbon atom. At the same time, nitrogen doping leads to an increased electrical conductivity due to electron excess in the delocalised p-system. Thus, the electrical conductivity and the number and the nature of the active sites are two important factors determining the performance of nitrogen-doped carbons in the ORR. Herein, N-doped nanocarbon/graphene composites were carefully designed, synthesized, characterized and tested as electrocatalysts in the ORR in order to decouple these two factors and investigate the underlying relationships between them. Chitosan was used as a nitrogen precursor for nanocarbon, while reduced graphene oxide was introduced to tune the electrical conductivity. Our results show that a low conductivity limits the exertion of active sites and results in a conductivity-dependent ORR activity. However, when the conductivity reaches a critical value, the active sites can be fully utilized and contribute to a positively correlated ORR activity.

Received 1st June 2016
Accepted 18th July 2016

DOI: 10.1039/c6ta04578b

www.rsc.org/MaterialsA

1. Introduction

The oxygen reduction reaction (ORR) plays a critical role in fuel cells and many other systems, such as metal–air batteries and oxygen sensors.^{1–4} The ORR process involves a multi-step proton-coupled electron transfer and high-energy barriers for the initial oxygen adsorption and O–O bond breaking, resulting in sluggish kinetics and low efficiencies.^{5,6} Effective catalysts are required to accelerate the ORR towards a lower onset potential, a higher saturated current density, and an improved long-term stability.^{7,8} Metallic Pt and Pt-based alloys are considered the best performing and efficient electrocatalysts. However, the high cost, scarcity, unfavourable geographic distribution, and poor stability severely hinder the large-scale application of Pt in these fields.⁸ Therefore, the development of Pt-free

electrocatalysts for the ORR with considerable catalytic activity and improved durability is highly desirable.

The ideal electrocatalyst for the ORR requires a conductive and porous framework to facilitate electron transfer and mass/gas diffusion at the interface between the electrolyte, active sites, and gas phase. In addition, effective and fully accessible active sites are required for superior catalytic activity. Heteroatom-doped carbon materials, in particular nitrogen-doped carbons (NCs), have been recently considered as promising alternatives to Pt. Such metal-free electrocatalysts present several advantages such as low cost, tuneable pore structure, adjustable surface chemistry, and high electrical conductivity.^{9–19} The excellent activity of NC is ascribed to the nitrogen incorporation into the carbon matrix with a modulated distribution of charge density, which results in a favourable adsorption or effective reduction of O₂.^{20,21} Therefore, the nature and the amount of N-containing active sites play a significant role in the ORR performance.^{4,20,21} The effect of the carbon matrix is also very important, influencing the electrical conductivity,¹⁴ length-to-width ratio,²² topological defects,^{23,24} surface roughness,²⁵ particle size, etc.²⁶ However, the synergistic role of the carbon framework coupled with heteroatom (nitrogen) doping effects in the ORR has thus far not been investigated.

The major obstacle is the difficulty in simultaneously controlling both the structural features of the carbon matrix

^aSchool of Engineering and Materials Science, Queen Mary University of London, London, E1 4NS, UK. E-mail: m.m.titirici@qmul.ac.uk

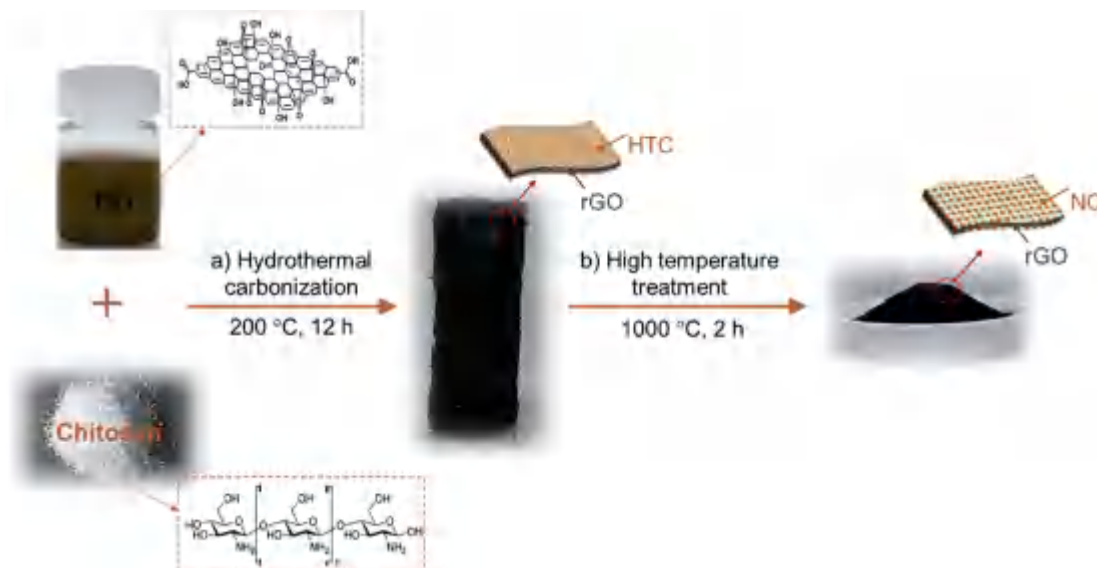
^bBeijing Key Laboratory of Green Chemical Reaction Engineering, Department of Chemical Engineering, Tsinghua University, Beijing, 100084, China

^cMaterials Chemistry Centre, Department of Chemistry, University College London, London, WC1H 0AJ, UK

^dMaterials Research Institute, Queen Mary University of London, London, E1 4NS, UK

† Electronic supplementary information (ESI) available. See DOI: 10.1039/c6ta04578b

‡ M. Qiao and C. Tang contributed equally to this work.



Scheme 1 Preparation of NC/rGO composites. (a) Hydrothermal carbonization of the mixture of GO and chitosan at 200 °C for 12 h. (b) After washing and freeze drying, the as-obtained material was annealed at 1000 °C for 2 h.

and the characteristics of the nitrogen dopants. Herein, we propose a carbon–carbon hybrid structure to demonstrate the different roles of the active sites and the carbon matrix. These composites are based on chitosan-derived NC shells hybridized with conductive graphene frameworks (Scheme 1). Chitosan, an abundant and renewable biomass material, is employed to generate N-containing active sites via the hydrothermal carbonization (HTC) process.^{25,27} Graphene oxide (GO) with an ultra-thin lamellar structure and rich in functional surface groups is introduced as a multi-functional substrate first to anchor the chitosan precursors, direct their carbonization, and help the resultant NC shells to adhere onto the graphene sheets (Scheme 1a). A series of nanocomposites with tuneable electrical conductivity and nitrogen-containing active sites are thus produced by carefully adjusting the mass ratio between chitosan and GO. The addition of graphene improves the conductivity, but simultaneously decreases the net amount of active sites derived from the nitrogen precursor.

2. Experimental section

2.1. Electrocatalyst fabrication

Chitosan (CS, medium molecular weight), graphite flakes, acetic acid (HAc, ACS reagent) and all the other chemicals used in this work were purchased from Sigma (UK). Deionized water was used for all the experiments. Graphene oxide (GO) in this contribution was prepared via a modified Hummer's method.^{28,29} Then, the synthesis procedure included two steps: hydrothermal carbonization (HTC) and high temperature carbonation process. During the HTC, CS and GO of different mass ratios were dissolved in 2.0% (v/v) acetic acid to achieve a homogeneous solution. The mixtures were then sealed into stainless steel autoclaves with a Teflon inlet and heated at 200 °C for 12 h under self-generated pressures of around 10 bars. After cooling to room temperature, the samples were

then frozen at –20 °C and then freeze dried for 72 hours. The products obtained from the HTC process are denoted as NC, NCG0.05, and NCG0.25, respectively. The number refers to the mass ratio of GO in the mixture of GO/CS. The as-obtained products were then annealed at 1000 °C under a N₂ flow for 2.0 h. The resultant samples were named as NC-1000, NCG0.05-1000, and NCG0.25-1000. Detailed compositions of the precursors and products are listed in Table 1. Pure rGO was synthesized under the same conditions for comparison.

2.2. Characterization

The morphology and structure of the samples were characterized using an FEI Inspect-F scanning electron microscope (SEM) and a JEM 2010 (JEOL Ltd., Tokyo, Japan) transmission electron microscope (TEM). Energy dispersive spectroscopy (EDS) analysis was performed at an acceleration voltage of 120.0 kV using a JEM 2010 (JEOL Ltd., Tokyo, Japan) TEM equipped with an Oxford Instrument energy dispersive spectrometer. The N₂ adsorption–desorption isotherm was measured using an Autosorb-IQ2-MP-C system (Quantachrome Instruments, USA). The specific surface area was calculated by the multipoint Brunauer–Emmett–Teller (BET) method, and the pore-size distribution was calculated based on Quenched Solid Density Function Theory (QSDFT) using the adsorption branch. X-ray photoelectron spectroscopy (XPS) was conducted on a Thermo Scientific K-alpha photoelectron spectrometer. Fourier-transform infrared (FTIR) spectroscopy was conducted on a Tensor 27.

2.3. Electrical conductivity test

For the four-probe electrical conductivity test, each sample was first pressed onto an adhesive, insulate substrate with a mass loading of 9 tons for 5 min to obtain a circular tablet with

a diameter of 13 mm. The as-prepared tablet was then measured in a four-point probe apparatus at room temperature.

Electrochemical impedance spectroscopy (EIS) measurements were conducted under 1600 rpm and at the potential under which the current density reaches 3 mA cm^{-2} for each sample. The amplitude is 10 mV.

2.4. Electrocatalytic performance measurements

In an ORR test, the electrode loading materials were prepared by mixing 1.8 mg catalyst, 264 mL ethanol, 700 mL H_2O , and 36 mL Nafion solution (5% w/w). The mixture was then sonicated for 40 min to obtain a homogeneous slurry and then 5 mL and 14 mL of the slurry were deposited on a glassy carbon (GC) rotating disk electrode (RDE) and a rotating ring-disk electrode (RRDE), respectively, followed by drying for 40 min at room temperature under air to obtain the working electrode. The diameters of glassy carbon disks of the RDE and RRDE are 3 mm and 5 mm, respectively. Therefore, the RDE and RRDE have the same mass loading of electrocatalyst per unit area.

All tests were performed on an electrochemical workstation (Metrohm Autolab PGSTAT204), using a standard three-electrode cell, where Ag/AgCl in 3 M AgCl-KCl solution served as the reference electrode and platinum wire as the counter electrode. The catalyst loading was ca. 0.127 mg cm^{-2} . Pt/C (20 wt%, Sigma-Aldrich, 738549) was prepared as electrodes for comparison with the same loading.

The ORR test was undertaken in 0.10 M KOH solution. Cyclic voltammetry (CV) was performed in nitrogen and oxygen-saturated electrolytes, at a scan rate of 100.0 mV s^{-1} . Linear sweep voltammograms (LSVs) were obtained at a rotation rate of 1600 rpm and a scan rate of 10 mV s^{-1} . The onset potential is determined as the potential required for a current density of -2 mA cm^{-2} (vs. RHE).

For the RRDE test, 0.10 M KOH solution was used as the electrolyte while a scan rate of 10 mV s^{-1} was applied within the same potential range as that for the RDE. The ring potential was held at 1.5 V vs. RHE to oxidize any H_2O_2 produced during the reaction. The working electrode is composed of a 5 mm GC disk electrode with a Pt ring electrode (375 mm gap). The following equation was used to calculate the percentage of H_2O_2 released during the reaction:

$$\% \text{H}_2\text{O}_2 = 100 \frac{2I_{\text{R}}/N}{I_{\text{D}} + (I_{\text{R}}/N)}$$

where I_{R} refers to the faradaic current at the ring, I_{D} is the faradaic current at the disk, N is the H_2O_2 collection coefficient at the ring, which was provided by the manufacturer, and N is 0.249 for this RRDE working electrode.

The stability of the catalyst was obtained by current-time chronoamperometric responses measured on the RDE electrode at peak potential in CV curves at a rotation speed of 800 rpm.

3. Results and discussion

3.1. Structure and surface chemistry of electrocatalysts

A family of NC/rGO composite electrocatalysts were thus fabricated with a GO mass content ranging from 0 to 25% (Table 1).

Table 1 Detailed composition of the precursors and products

| Sample | Composition (mass ratio) | Chitosan (mg mL^{-1}) | GO (mg mL^{-1}) | HAc (v/v) |
|--------------|--------------------------|----------------------------------|----------------------------|-----------|
| NC | Pure CS | 60.0 | 0 | 2% |
| NCG0.05 | 95% CS + 5% GO | 60.0 | 3.0 | 2% |
| NCG0.25 | 75% CS + 25% GO | 9.0 | 3.0 | 2% |
| NC-1000 | — ^a | 60.0 | 0 | 2% |
| NCG0.05-1000 | — ^a | 60.0 | 3.0 | 2% |
| NCG0.25-1000 | — ^a | 9.0 | 3.0 | 2% |

^a The composition of high-temperature annealed samples is determined by the HTC products.

The as-obtained products are denoted as NC/graphene composites (NCG): NC, NCG0.05, and NCG0.25, respectively. During the hydrothermal process, under subcritical conditions at $200 \text{ }^\circ\text{C}$, the GO is converted to reduced graphene oxide (rGO) with high electrical conductivity while the chitosan is hydrothermally carbonised to NC. The HTC process of chitosan ends up obtaining nitrogen-derived particles with oxygen-containing hydrophilic functional groups, which make it very accessible for the hybridization process.^{30–32} The sequential high-temperature treatment under an inert atmosphere improves the graphitization degree of NC leading to different types of hybrid carbon-carbon materials with distinctive surface chemistries and properties (Scheme 1b). The as-obtained products are denoted as NC/graphene composites (NCG): NC, NCG0.05, and NCG0.25, respectively.

Fig. 1 shows the morphology and microstructure of the samples characterized by scanning and transmission electron microscopy (SEM and TEM). The pristine NC obtained through the hydrothermal carbonization of chitosan exhibits irregular spherical particles, in good agreement with previous reports (Fig. 1a).³³ With the addition of GO, the composites show completely different morphologies (Fig. 1b and c). The introduction of 5% GO leads to large flat agglomerates around 10 nm whereby the NC particles are uniformly anchored on both sides of the GO sheets (Fig. 1b). The size of NC particles in NCG0.05 is smaller than those in pristine samples (Fig. 1a), indicating that the GO also acts as a stabiliser during the HTC process. The polar functional groups on the GO surface interact with the chitosan precursors and subsequently carbonize on the resulting rGO structure; consequently there are very few free NC particles in NCG0.05 (Fig. 1b). When the GO amount was increased to 25%, the resultant sample exhibits a similar morphology to pristine rGO, without any obvious NC particles (Fig. 1c and S1†). In this case, a thin layer of nitrogen-doped carbon was coated onto GO. This has been previously observed during the hydrothermal carbonisation of carbohydrates in the presence of inorganic particles when the concentration of the carbohydrate is low compared with that of the inorganic material to be carbon coated.¹¹

After further high-temperature annealing under a N_2 atmosphere at $1000 \text{ }^\circ\text{C}$, all samples maintain their overall morphologies; however the NC particles in NC and NCG0.05 are visibly shrunk (Fig. 1d–f).^{34,35} The corresponding products are denoted

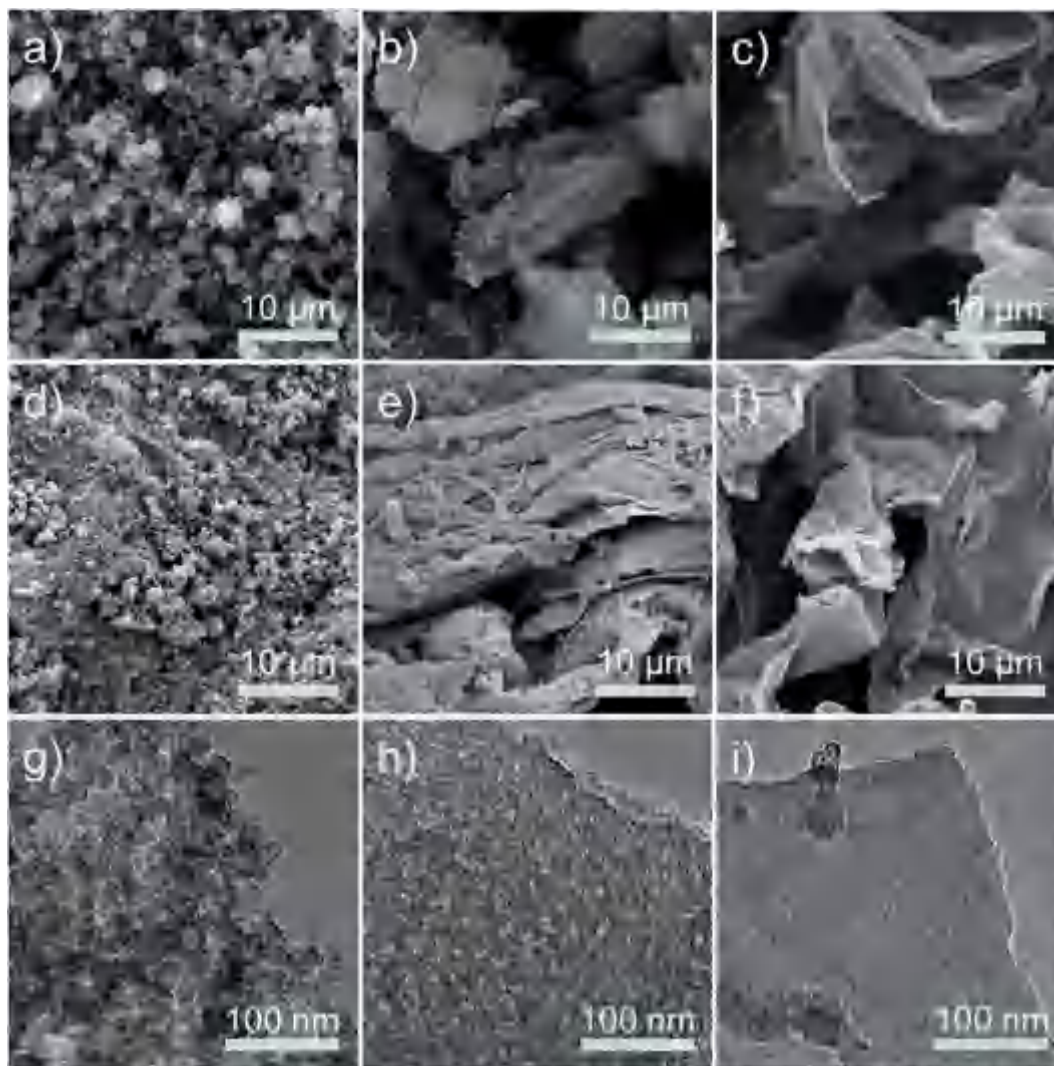


Fig. 1 SEM images of (a) NC, (b) NCG0.05, and (c) NCG0.25 obtained after the HTC process with different chitosan/GO ratios. SEM images of (d) NC-1000, (e) NCG0.05-1000, and (f) NCG0.25-1000 obtained after high-temperature treatment. TEM images of (g) NC-1000, (h) NCG0.05-1000, and (i) NCG0.25-1000 samples.

as NC-1000, NCG0.05-1000, and NCG0.25-1000, respectively. The TEM images further reveal their hierarchical structures (Fig. 1g–i). NC particles with a size of ca. 20 nm are interconnected into a porous framework (Fig. 1g). With the presence of graphene sheets, however, porous NC shells are coated on GO and exhibit the laminar structure like rGO (Fig. 1h and i and S1b†).

The final yields support the fact that a strong interaction occurs between the two components during the hydrothermal treatment. As shown in Table S1,† the yield of NCG from the GO and chitosan mixed system is higher, compared with the result summed up from monocomponent systems of GO and chitosan. This suggests that there is an interaction between the GO and chitosan during the HTC process and that the laminar structure and surface functionalities of the GO facilitate the transformation of chitosan during this process. FTIR spectra reveal no obvious shifts of the band position (Fig. S2†), demonstrating a similar chemical bond composition in NC,

NCG0.05 and NCG0.25. However, relative strength of the band varied at around 800 cm^{-1} at $1250\text{--}1600\text{ cm}^{-1}$, which corresponds to the triazine ring vibration and stretching modes of the heterocyclic CN,^{36,37} respectively. This indicates that the introduction of GO directs the assembly process of NC shells, resulting in a varied proportion of C–N bonds, but did not change the type of chemical bond.

The introduction of graphene improves the electrical conductivity (Table 2). For the pristine NC sample, the electrical conductivity is too low to be determined by the four-probe method. With the addition of GO, the conductivity increases to 0.05 S m^{-1} for NCG0.05 and 29.2 S m^{-1} for NCG0.25. GO has been partially reduced into rGO during HTC treatment, which provides a conductive skeleton for the composites. After high-temperature treatment, all samples display improved electrical conductivity due to the “graphitization” of the hydrothermal carbons. A similar tendency can be obtained in

Table 2 Electrical conductivity of different samples measured by the four-probe method

| Sample | NC | NCG0.05 | NCG0.25 | NC-1000 | NCG0.05-1000 | NCG0.25-1000 |
|------------------------------|-----|---------|---------|---------|--------------|--------------|
| Conductivity ($S\ m^{-1}$) | N/A | 0.05 | 29.2 | 6.5 | 12.0 | 57.6 |

impedance testing for high temperature treated samples (Fig. S3†).

Energy dispersive spectroscopy (EDS) mapping of NCG0.25-1000 demonstrates a uniform distribution of nitrogen and carbon elements, demonstrating indeed that rGO sheets are covered by the NC shells (Fig. 2a–c). X-ray photoelectron spectroscopy (XPS) analysis was performed to further investigate the nitrogen incorporation into NCG composites (Table S2†). High-resolution XPS spectra of N 1s peaks are presented in Fig. 2d and e. For HTC products, the total nitrogen contents are

4.50 ± 1.00 at%, and the bonding states can be assigned to three dominant configurations: pyridinic-N (ca. 398 eV), pyrrolic-N (ca. 400 eV) and quaternary-N (ca. 401 eV), respectively.^{38,39} It is notable that the contents of both total nitrogen, quaternary-N and pyrrolic-N are increased after the introduction of GO (NCG0.05), which demonstrates that indeed the GO influences the hydrothermal carbonization of chitosan and the nitrogen incorporation into the carbon matrix (Table S2†). Further addition of GO (NCG0.25) decreases the amount of nitrogen dopants due to the net reduction of nitrogen precursors. After

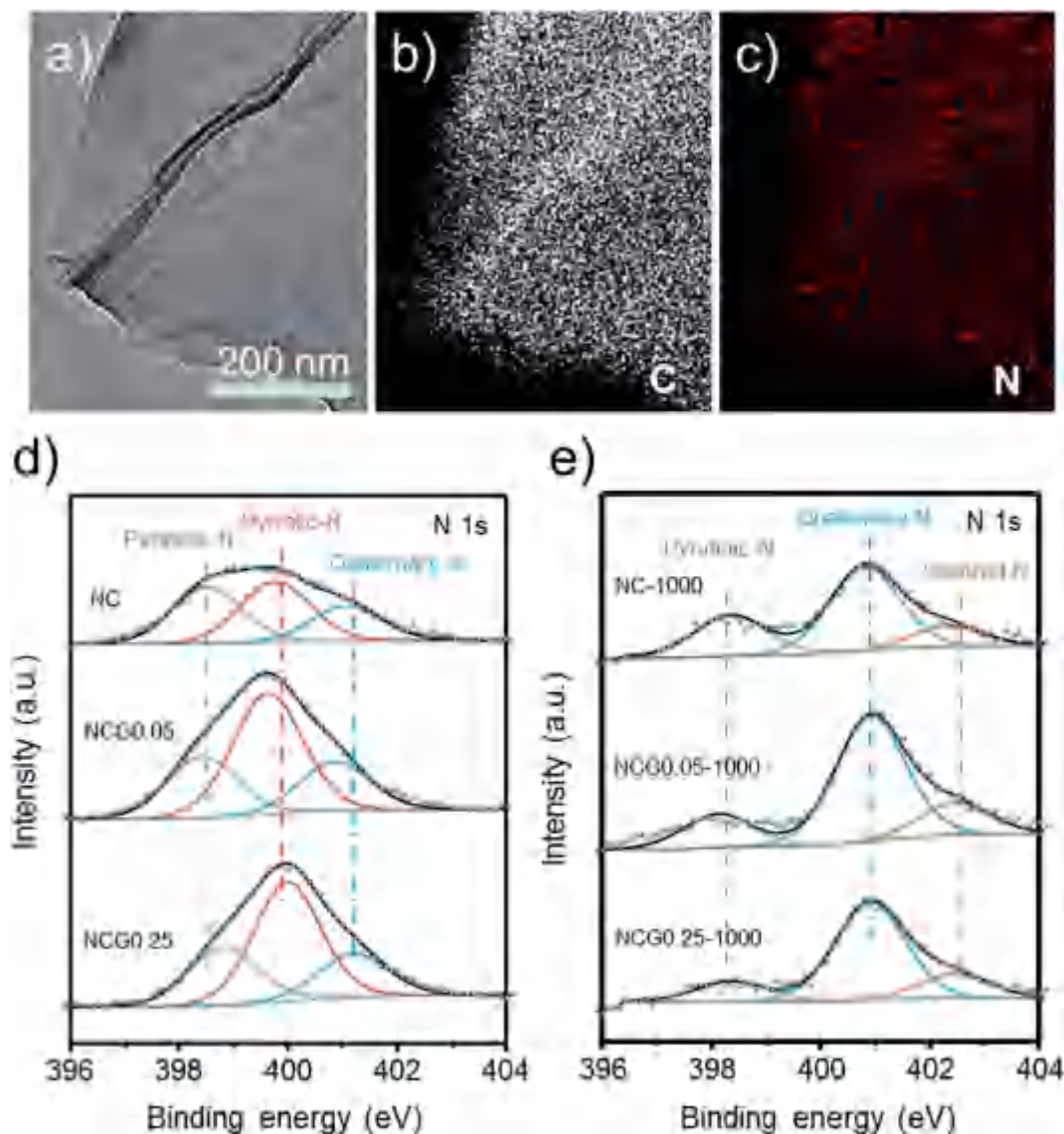


Fig. 2 (a) TEM image of NCG0.25-1000 and the corresponding EDS mapping, showing the uniform distribution of (b) C and (c) N elements. The high-resolution N 1s spectra of samples obtained (d) after HTC or (e) after high-temperature annealing.

the high-temperature annealing, the nitrogen contents decreased to 1.45 ± 0.20 at%, with an obvious decrease of pyridinic N, disappearance of pyrrolic N and generation of oxidized-N (>402 eV). It has been reported that both pyrrolic and pyridinic structures are unstable at high temperature and tend to transform into a more stable quaternary nitrogen configuration.^{40,41} Besides, the oxidized-N, such as pyridinic-N⁺-O⁻, is considered as a stable configuration,⁴¹ which is ascribed to the reaction between nitrogen dopants and oxygen-containing functional groups of GO during annealing.

High-temperature treatment not only regulates the configuration of nitrogen, but also modulates the graphitization degree and porosities. High-resolution TEM (HRTEM) images of the NC particles in NC-1000 are presented in Fig. 3a indicating the amorphous carbon structure. However, after annealing for 2 h, distinct graphitic layers or graphene rings with a diameter of several nanometers are observed (Fig. 3b), which are remarkably different from the HTC products. Functional groups are mostly removed during the high temperature carbonization step, while the amorphous structure is transformed into a more graphitized structure. Porosity and BET surface areas of different samples were evaluated using nitrogen sorption at -196 °C by the Density Functional Theory (DFT) method (Fig. 3c and d and S4†). The

specific surface area (SSA) of HTC products significantly increases after annealing along with the total pore volume (Table S3†). Upon further carbonization at high temperature, mesopores of around 6 nm demonstrate a peak distribution (Fig. 3c and d), which is consistent with the HRTEM results (Fig. 3a and b). The BET surface area and pore volume values of NC or NCG0.25 are increased more than ten-fold after annealing. This change is ascribed to the structural transformation of NC shells derived from chitosan as supported by TEM. NCG0.05-1000 exhibits the highest BET surface area, 338 m² g⁻¹ and a high pore volume of 0.9 cm³ g⁻¹. The BET surface area and pore volume of NCG0.05 are about ten and five times higher than those of both NC and NCG0.25, respectively. This is most likely due to the fact that GO sheets help a good dispersion of NC particles leading to a smaller particle size during the hydrothermal reaction (Fig. 1b). Additionally, the NC shells anchored on GO can effectively restrain the restacking of graphene sheets, resulting in a higher BET area and pore volume after pyrolysis. In the case of NCG0.25, since the NC deposited on graphene is very thin, there is little effect on the BET surface area and pore volume in comparison with NCG0.05 (Fig. 1c).

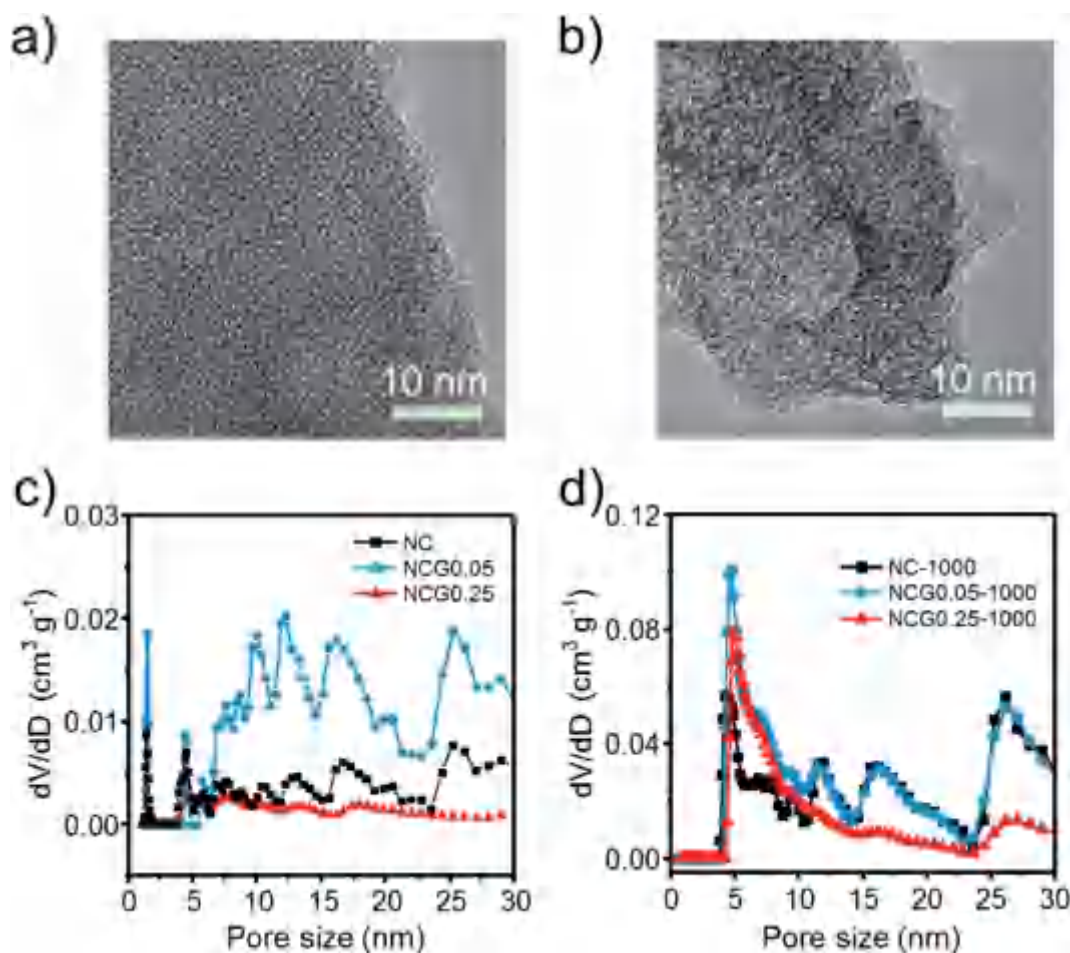


Fig. 3 HRTEM image of (a) the NC sample and (b) NC-1000 sample. The pore size distribution of different samples obtained after (c) HTC and (d) after annealing.

3.2. ORR performance

The ORR electrocatalytic activities of various NC/rGO composites were measured in an alkaline solution (0.10 M KOH). A commercial Pt/C catalyst (20 wt% loading, Sigma) was also measured under the same conditions for comparison (Fig. S5†). The cyclic voltammetry (CV) curves recorded in both O₂ and N₂ saturated electrolytes are shown in Fig. 4a. In the presence of O₂, distinct ORR responses were observed on all samples in contrast to the quasi-rectangular voltammograms for N₂-saturated solution, suggesting their good reactivity for the ORR. It is notable that the peak potential of NCG0.25 is positively shifted by 48 mV, compared with that of NC. After high-temperature annealing, however, the NC-1000 sample exhibits the lowest overpotential and highest peak current density, clearly indicating its excellent catalytic activity even without any graphene addition (Table S4†).

To further investigate the ORR activity and underlying mechanism, linear sweep voltammetry (LSV) was performed using a rotating disk electrode (RDE) with a rotation rate of 1600 rpm. As shown in Fig. 4b, all the annealed samples substantially outperform the HTC samples with respect to both overpotential and current density. Increasing GO addition resulted in more positive onset potential and higher diffusion-limited current density (J_D) relative to the HTC products. The onset potential of NCG0.25 is ca. 90 mV higher than that of NC, while the current density (J_D) gradually increased from 1.57, 1.75 to 1.85 mA cm⁻², for NC, NCG0.05 and NCG0.25, respectively. In the case of annealed samples, however, the ORR performance shows negative correlation with the graphene content. Unexpectedly, the NC-1000 exhibits the best ORR activity with an onset potential of ca. 993 mV, which is

dramatically shifted from 832 mV of the NC sample. Besides, the J_D is more than twice that of NC. The LSV curve of NCG0.25-1000 still exhibits an obvious two-plateau peroxide pathway, with a slightly increased current density but even lower onset potential. It indicates a tiny role of the high-temperature treatment for NCG0.25, in contrast to NC. LSV curves of NCG0.25 and NC-1000 at different rotation speeds are shown in Fig. S6.† Current-time chronoamperometric responses (Fig. S7†) were measured at peak potential in CV curves as shown in Fig. 4a. The NC-1000 shows improved stability compared with NC; both demonstrate better stability than the commercial Pt-C catalyst.

The peroxide yield was calculated to evaluate the amount of H₂O₂ generated during the ORR (Fig. 5 and S8†). All samples show a H₂O₂ yield higher than 20%, while NCG0.25 shows a lowest H₂O₂ yield of around 29%, which is superior to NCG0.05 and NC which show a H₂O₂ yield of around 47% and 40%, respectively. For the further carbonised samples, NCG0.25-1000 exhibited a distinctive increase in the H₂O₂ yield of around 61%.

3.3. The relationship between the ORR performance and electrocatalyst

Detailed structure-performance investigations are carried out to rationalize this observation (Fig. 4c and 5 and Table S5†). Both electrical conductivity and catalytically active sites are two critical parameters for metal-free carbon based electrocatalysis.¹⁴ Nitrogen-induced active sites are responsible for the ORR activity of NC materials, although the exact mechanisms of this are still under debate. The increase in graphene content enhances the electrical conductivity, while the net amount of NC derived from chitosan is reduced.

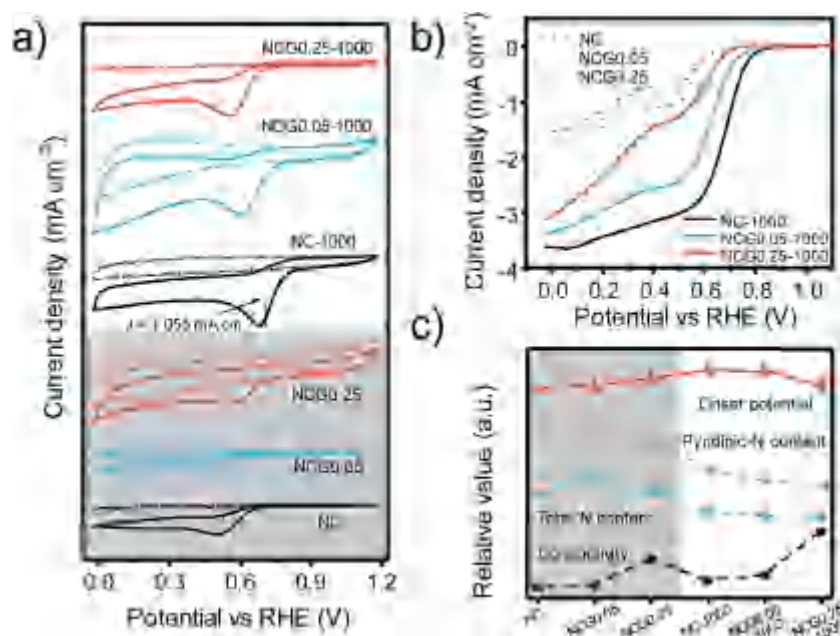


Fig. 4 (a) CV curves of different samples in N₂ (dot) or O₂-saturated (line) 0.10 M KOH solution. The scan rate was 100.0 mV s⁻¹. (b) LSV curves of different samples in O₂-saturated 0.10 M KOH solution with a rotation rate of 1600 rpm. The scan rate was 10.0 mV s⁻¹. (c) The comparison between performance and material properties, such as conductivity, total N content, and pyridinic-N content. The catalyst loading was ca. 0.127 mg cm⁻² for all measurements.

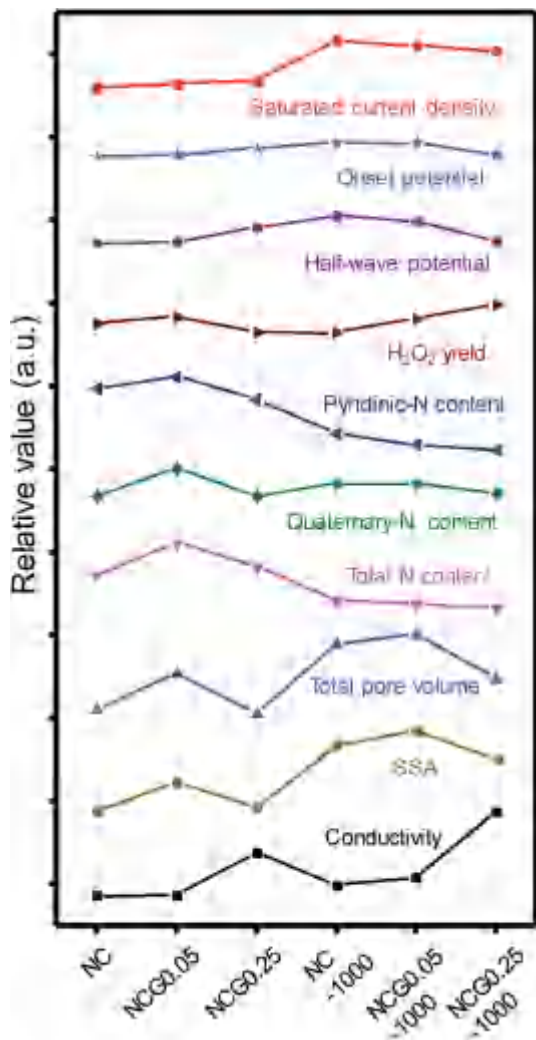


Fig. 5 Detailed comparison between ORR performance and material properties.

The electrical conductivity of the hydrothermal carbons is so low that it largely limits the electron transport during catalysis, inhibiting the contribution from nitrogen-doped active sites and restricting the overall ORR activity. NCG0.05 is clearly inferior to NCG0.25 in ORR performance, although it has more nitrogen heteroatom dopants, higher SSA and larger pore volumes (Table S5†). On the other hand, once the electrical conductivity reaches a certain threshold, after additional high-temperature treatment, the active nitrogenated sites become the key factor indicating the material's ORR performance. The current density, onset potential and half-wave potential are considerably increased, as now the electronic conductivity facilitates the transport to the active sites for electron transfer. In the case of the high temperature samples, the variation of J_D , onset potential and half-wave potential follows the exact trend dictated by the nitrogen content, independent of conductivity. The NC-1000 with no GO but with the highest nitrogen content performs better than NCG0.05-1000 and NCG0.25-1000. Notably, the amount of pyridinic-N can be nicely correlated with onset potential and half-wave potential (Fig. 4c and 5),

indicating the intrinsic activity of pyridinic-type nitrogen heteroatoms in good agreement with previous reports.^{15,42}

Although the influence of active sites and electrical conductivity on the H_2O_2 yield is still under debate, in this case it is surprising to see that the H_2O_2 yield for both hydrothermally carbonised and further carbonized samples follows a very similar trend to that of J_D , onset potential and half-wave potential. The H_2O_2 yield of NCG 0.25 is less than that of NC and NCG0.05, while NC-1000 shows a substantially reduced H_2O_2 yield compared to NCG0.05-1000 and NCG0.25-1000, in good agreement with the variation of electrical conductivity.

4. Conclusions

We have fabricated a series of NC/rGO hybrids and demonstrated the different roles of both the active sites and the conductivity of the carbon matrix towards ORR performance. The chitosan-derived NC shells induced the formation of abundant active sites while reduced graphene oxide sheets prompt electrical conductivity. After high-temperature treatment, the nitrogen dopants were partly removed while the remaining ones transformed into more stable structures (pyridinic-N and oxidized-N), and the conductivity of composites is enhanced above a critical value. Low electrical conductivity limits access to the active sites. However, the amount and type of active site are the main contributors to ORR activity when conductivity is no longer a limitation. The main conclusion of the study is that conductive additives, such as graphene, can improve some of the properties and performance of nitrogen doped carbons derived from biomass precursors but they can also bring about side effects, which should be carefully investigated.

Acknowledgements

This work was supported by funding from the Natural Scientific Foundation of China (No. 21422604 and 21561130151). Q. Z. and M. M. T. thank the Royal Society for the award of a Newton Advanced Fellowship (Ref: NA140249). M. Qiao and G. He are grateful to the Chinese government for the award of CSC scholarships.

References

- 1 A. Zehtab Yazdi, H. Fei, R. Ye, G. Wang, J. Tour and U. Sundararaj, *ACS Appl. Mater. Interfaces*, 2015, 7, 7786–7794.
- 2 J. Zhu, G. He, L. Liang, Q. Wan and P. K. Shen, *Electrochim. Acta*, 2015, 158, 374–382.
- 3 B. Xia, Y. Yan, X. Wang and X. W. Lou, *Mater. Horiz.*, 2014, 1, 379–399.
- 4 L. M. Dai, Y. H. Xue, L. T. Qu, H. J. Choi and J. B. Baek, *Chem. Rev.*, 2015, 115, 4823–4892.
- 5 Y. Jiao, Y. Zheng, M. T. Jaroniec and S. Z. Qiao, *Chem. Soc. Rev.*, 2015, 44, 2060–2086.
- 6 G. Yang, W. Choi, X. Pu and C. Yu, *Energy Environ. Sci.*, 2015, 8, 1799–1807.

- 7 G. L. Tian, M. Q. Zhao, D. Yu, X. Y. Kong, J. Q. Huang, Q. Zhang and F. Wei, *Small*, 2014, 10, 2251–2259.
- 8 Y. Nie, L. Li and Z. Wei, *Chem. Soc. Rev.*, 2015, 44, 2168–2201.
- 9 J. Liang, X. Du, C. Gibson, X. W. Du and S. Z. Qiao, *Adv. Mater.*, 2013, 25, 6226–6231.
- 10 D.-W. Wang and D. Su, *Energy Environ. Sci.*, 2014, 7, 576.
- 11 L. T. Qu, Y. Liu, J. B. Baek and L. M. Dai, *ACS Nano*, 2010, 4, 1321–1326.
- 12 Y. Ito, H. J. Qiu, T. Fujita, Y. Tanabe, K. Tanigaki and M. W. Chen, *Adv. Mater.*, 2014, 26, 4145–4150.
- 13 J. Liang, Y. Zheng, J. Chen, J. Liu, D. Hulicova-Jurcakova, M. Jaroniec and S. Z. Qiao, *Angew. Chem., Int. Ed.*, 2012, 51, 3892–3896.
- 14 S. B. Yang, X. L. Feng, X. C. Wang and K. Mullen, *Angew. Chem., Int. Ed.*, 2011, 50, 5339–5343.
- 15 D. S. Geng, Y. Chen, Y. G. Chen, Y. L. Li, R. Y. Li, X. L. Sun, S. Y. Ye and S. Knights, *Energy Environ. Sci.*, 2011, 4, 760–764.
- 16 Z. J. Lu, S. J. Bao, Y. T. Gou, C. J. Cai, C. C. Ji, M. W. Xu, J. Song and R. Y. Wang, *RSC Adv.*, 2013, 3, 3990–3995.
- 17 K. P. Gong, F. Du, Z. H. Xia, M. Durstock and L. M. Dai, *Science*, 2009, 323, 760–764.
- 18 D. S. Yu, Q. Zhang and L. M. Dai, *J. Am. Chem. Soc.*, 2010, 132, 15127–15129.
- 19 J. Zhang and L. Dai, *ACS Catal.*, 2015, 5, 7244–7253.
- 20 D. W. Wang and D. S. Su, *Energy Environ. Sci.*, 2014, 7, 576–591.
- 21 L. Dai, Y. Xue, L. Qu, H.-J. Choi and J.-B. Baek, *Chem. Rev.*, 2015, 115, 4823–4892.
- 22 M. W. Chung, C. H. Choi, S. Y. Lee and S. I. Woo, *Nano Energy*, 2015, 11, 526–532.
- 23 G. L. Chai, Z. F. Hou, D. J. Shu, T. Ikeda and K. Terakura, *J. Am. Chem. Soc.*, 2014, 136, 13629–13640.
- 24 L. Tao, Q. Wang, S. Dou, Z. Ma, J. Huo, S. Wang and L. Dai, *Chem. Commun.*, 2016, 52, 2764–2767.
- 25 M. K. Rybarczyk, M. Lieder and M. Jablonska, *RSC Adv.*, 2015, 5, 44969–44977.
- 26 J. Duan, S. Chen, M. Jaroniec and S. Z. Qiao, *ACS Catal.*, 2015, 5, 5207–5234.
- 27 Z. H. Zhang and P. Y. Wu, *RSC Adv.*, 2014, 4, 45619–45624.
- 28 G.-P. Hao, A.-H. Lu, W. Dong, Z.-Y. Jin, X.-Q. Zhang, J.-T. Zhang and W.-C. Li, *Adv. Energy Mater.*, 2013, 3, 1421–1427.
- 29 W. S. Hummers and R. E. Offeman, *J. Am. Chem. Soc.*, 1958, 80, 1339–1339.
- 30 B. Hu, K. Wang, L. H. Wu, S. H. Yu, M. Antonietti and M. M. Titirici, *Adv. Mater.*, 2010, 22, 813–828.
- 31 M. M. Titirici and M. Antonietti, *Chem. Soc. Rev.*, 2010, 39, 103–116.
- 32 M. M. Titirici, R. J. White, N. Brun, V. L. Budarin, D. S. Su, F. del Monte, J. H. Clark and M. J. MacLachlan, *Chem. Soc. Rev.*, 2015, 44, 250–290.
- 33 L. Zhao, L.-Z. Fan, M.-Q. Zhou, H. Guan, S. Qiao, M. Antonietti and M.-M. Titirici, *Adv. Mater.*, 2010, 22, 5202–5206.
- 34 J. Popovic, R. Demir-Cakan, J. Tornow, M. Morcrette, D. S. Su, R. Schlogl, M. Antonietti and M. M. Titirici, *Small*, 2011, 7, 1127–1135.
- 35 R. Demir Cakan, M. M. Titirici, M. Antonietti, G. Cui, J. Maier and Y. S. Hu, *Chem. Commun.*, 2008, 3759–3761, DOI: 10.1039/b805671b.
- 36 J. Zhang, L. Qu, G. Shi, J. Liu, J. Chen and L. Dai, *Angew. Chem.*, 2016, 55, 2230–2234.
- 37 X. Fu, X. Hu, Z. Yan, K. Lei, F. Li, F. Cheng and J. Chen, *Chem. Commun.*, 2016, 52, 1725–1728.
- 38 J. R. Pels, F. Kapteijn, J. A. Moulijn, Q. Zhu and K. M. Thomas, *Carbon*, 1995, 33, 1641–1653.
- 39 L. Roldan, S. Armenise, Y. Marco and E. Garcia-Bordeje, *Phys. Chem. Chem. Phys.*, 2012, 14, 3568–3575.
- 40 K. Stanczyk, R. Dziembaj, Z. Piwowarska and S. Witkowski, *Carbon*, 1995, 33, 1383–1392.
- 41 G. Liu, X. G. Li, P. Ganesan and B. N. Popov, *Appl. Catal., B*, 2009, 93, 156–165.
- 42 L. F. Lai, J. R. Potts, D. Zhan, L. Wang, C. K. Poh, C. H. Tang, H. Gong, Z. X. Shen, L. Y. Jianyi and R. S. Ruoff, *Energy Environ. Sci.*, 2012, 5, 7936–7942.